

Wakefield-Induced Ionization injection in beam-driven plasma accelerators

A. Martinez de la Ossa,^{1,2} T. J. Mehrling,¹ L. Schaper,¹ M. J. V. Streeter,¹ and J. Osterhoff¹

¹⁾ *Deutsches Elektronen-Synchrotron DESY, D-22607 Hamburg, Germany*

²⁾ *Institut für Experimentalphysik, Universität Hamburg, D-22761 Hamburg, Germany*

(Dated: March 24, 2022)

We present a detailed analysis of the features and capabilities of Wakefield-Induced Ionization (WII) injection in the blowout regime of beam driven plasma accelerators. This mechanism exploits the electric wakefields to ionize electrons from a dopant gas and trap them in a well-defined region of the accelerating and focusing wake phase, leading to the formation of high-quality witness-bunches¹. The electron-beam drivers must feature high-peak currents ($I_b^0 \gtrsim 8.5$ kA) and a duration comparable to the plasma wavelength to excite plasma waves in the blowout regime and enable WII injection. In this regime, the disparity of the magnitude of the electric field in the driver region and the electric field in the rear of the ion cavity allows for the selective ionization and subsequent trapping from a narrow phase interval. The witness bunches generated in this manner feature a short duration and small values of the normalized transverse emittance ($k_p \sigma_z \sim k_p \epsilon_n \sim 0.1$). In addition, we show that the amount of injected charge can be adjusted by tuning the concentration of the dopant gas species, which allows for controlled beam loading and leads to a reduction of the total energy spread of the witness beams. Electron bunches, produced in this way, fulfil the requirements to drive blowout regime plasma wakes at a higher density and to trigger WII injection in a second stage. This suggests a promising new concept of self-similar staging of WII injection in steps with increasing plasma density, giving rise to the potential of producing electron beams with unprecedented energy and brilliance from plasma-wakefield accelerators.

PACS numbers: 52.40.Mj, 52.65.Rr, 52.25.Jm, 52.59.-f

I. INTRODUCTION

Beam driven plasma wakefield accelerators (PWFA)^{2,3} can generate and sustain accelerating gradients in excess of ~ 10 GV/m over meter-scale distances. This was proven in a landmark experiment at SLAC⁴, where the energy of the electrons in the tail of a 42 GeV electron beam was doubled within a distance of less than a meter, after being accelerated in the plasma wake, which was excited by the head of the beam. Harnessing such extreme fields for the production of multi-GeV energy, high-brightness electron beams will enable a new generation of accelerators, capable of compactly driving applications e.g. in particle physics, optics, medicine or materials science.

Improved control over the injection of beams into a suitable phase of the plasma wake is a necessary step towards the production of beams from plasma-based accelerators with a quality comparable to those generated in current state of the art particle accelerators. The first peaked electron beam spectra were obtained from laser driven plasma wakefield accelerators (LWFA)⁵ by uncontrolled nonlinear wavebreaking⁶⁻⁸. Subsequently, the implementation⁹⁻¹⁵ of earlier proposed¹⁶⁻¹⁹ controlled injection methods paved the way towards electron beams with improved tunability, stability and quality. The experimental realization of injection techniques in PWFA is not yet as developed as in LWFA, and only recently PWFA has been advanced from single-beam electron acceleration^{4,20} to the acceleration of distinct witness beams²¹. To obtain high-quality beams from PWFA, different injection techniques, based on density tailoring²², magnetic-induced trapping²³ or external witness bunch

generation²¹ have been proposed. A promising approach is the injection of electrons in plasma by means of field-induced ionization of a dopant gas with appropriate ionization potential^{24,25}. Injection from ionization, induced in a dopant gas by the radial electric field of the driving beam was first observed in an experiment²⁴ at FACET²⁶. That method is highly sensitive to details of the initial charge density distribution and the transverse emittance of the driving beam and is therefore not easily controlled and contingent on fluctuations of the beam structure. In addition, the injection of excessive charge can severely beam load the wake and may result in the production of a continuous current that distorts the wakefield²⁷ instead of a well defined witness beam. Laser-triggered ionization injection^{28,29} offers the possibility to control the volume of injection in a precise way. These methods rely on a high degree of spatial ($\sim 1 \mu\text{m}$) and temporal (~ 10 fs) alignment of the laser pulses with respect to the electron beam in order to induce ionization in the desired phase of the plasma wake and to produce high quality beams.

A novel ionization-based injection strategy, Wakefield-Induced Ionization (WII) injection, was recently proposed¹ as a method to achieve a high degree of control over the injection of electrons into the appropriate phase of the plasma wave. In contrast to the aforementioned methods, WII injection is neither sensitive to details of the beam structure, nor does it rely on additional devices, such as lasers, for the injection. Instead, it exploits the difference of the absolute electric-field strength between the accelerating and decelerating regions of the first wakefield bucket in the blowout regime³⁰⁻³² to selectively ionize a small volume of a background dopant gas near the phase of maximum acceleration. In this

way the production of high-quality, ultra-short (\sim fs), low-emittance ($\sim \mu\text{m}$), multi-GeV-energy electron beams from a comparably simple experimental setup is possible.

In this work, we present a detailed analysis of the features and capabilities of WII injection. Since the method relies on properties which are inherent in the structure of beam-driven blowout plasma wakes, we first review the phenomenology of PWFA in the blowout regime (Sec. II). The most important scalings are discussed there and compared to data from 3D simulations with the Particle-In-Cell (PIC) code OSIRIS^{33–35}. This analysis allows for a thorough determination of the requirements for WII injection. The injection principle is demonstrated in exemplary 3D simulations with OSIRIS, considering two realistic experimental scenarios for PWFA, namely the FLASHForward project at DESY (Sec. III) and the FACET experiment at SLAC (Sec. IV). WII injection also allows controlled beam-loading to reduce the total energy spread of the witness bunch (Sec. V). This results in the generation of compact, high-energy, low-emittance and high-current witness bunches, which fulfil all requirements to again trigger WII injection as driver beams in substantially higher density plasmas. This brings up a new concept of self-similar staging, which has the potential of producing electron beams with unprecedented energy and quality in PWFA (Sec. VI).

II. THEORY

PWFA use relativistic charged particle beams that are sufficiently dense to significantly displace the plasma electrons from their ions by means of the Coulomb force of its charge. As the beam passes, the displaced plasma electrons are attracted back by the excess of positive ions left behind, and oscillate around their equilibrium position, generating in this way a plasma density perturbation that is propagating at the velocity of the beam ($v_b \approx c$). For small displacements, these oscillations are harmonic at a frequency given by $\omega_p = \sqrt{n_0 e^2 / m \epsilon_0}$ and a wavelength of $\lambda_p = 2\pi / k_p = 2\pi c / \omega_p$, where n_0 is the plasma particle density, ϵ_0 is the vacuum permittivity, c the speed of light, and m and e are the electron mass and charge, respectively. High-current ($I_b \gtrsim 1$ kA), resonant-length ($L_b \approx \lambda_p$) and narrow ($k_p \sigma_r \lesssim 1$) electron drivers blow out all the plasma electrons from their propagation path, creating an ion cavity with no plasma electrons inside. As can be seen in PIC simulations (Figure 1 (a)), this ion-cavity (or blowout) is clearly delimited by a sheath of plasma electrons, which accumulate at a distance r_l from the propagation axis. The blowout regime features ideal properties for the acceleration and transport of compact electron bunches³⁰. Given the absence of radial currents inside the blowout (and assuming cylindrical symmetry), it can be directly shown from Maxwell equations that inside the ion cavity the transverse wakefields, $W_\perp \equiv E_r - cB_\phi$, depend linearly on the radius $W_\perp / E_0 = k_p r / 2$, and are constant along the

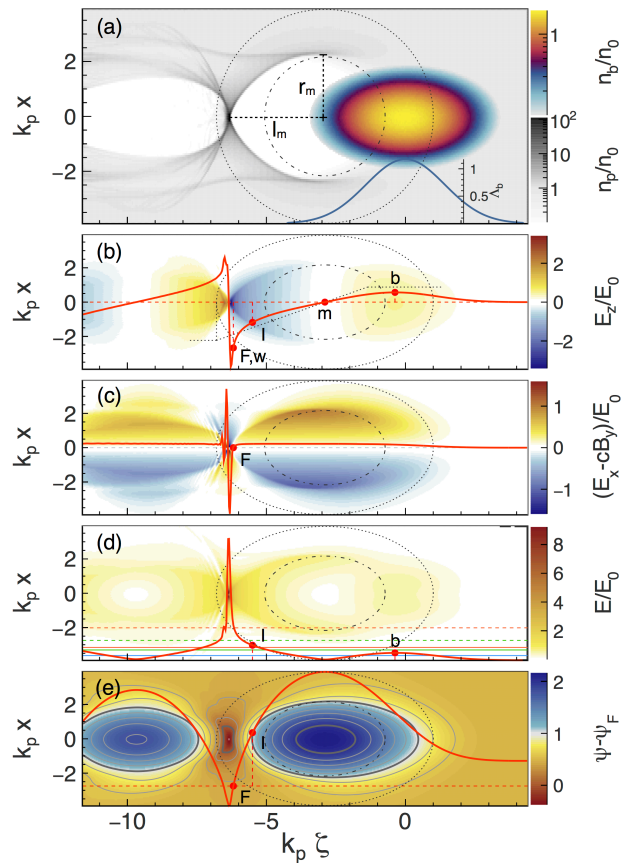


Figure 1. An OSIRIS 3D simulation of a high-current ($I_b = 10$ kA), moderately wide ($(k_p \sigma_r = 0.8)$), axially symmetric Gaussian electron beam, going through a plasma at the (linear) resonant length ($k_p \sigma_z = \sqrt{2}$). (a) Spatial particle density. (b) Longitudinal electric field. (c) Transverse electric field. (d) Electric field magnitude. (e) Wake potential. Red solid lines are the corresponding quantity along the on-axis region, except for (c) and (d), where the profile is taken $0.1 k_p^{-1}$ off-axis. The outer and inner circles represent the blowout radius estimations through Eq. (6b) and Eq. (9), respectively. The dark dotted lines in (b) indicate the model estimations for the maximum decelerating field in the beam region (right horizontal line, Eq. (6a)), the maximum accelerating field (left horizontal line, Eq. (8a)), and the longitudinal field slope around the center of the cavity (diagonal line, Eq. (7)).

co-moving variable $\partial_\zeta W_\perp = 0$, where the co-moving variable is defined as $\zeta = z - ct$ (see Figure 1 (c)); while the longitudinal wakefield, $W_z \equiv E_z$, is constant along the radius in the blowout, $\partial_r E_z = 0$ (see Figure 1 (b)). Here $E_0 \equiv k_p m c^2 / e$ is the cold non-relativistic wavebreaking field³⁶. The longitudinal structure of E_z , on the other hand, exhibits a substantial difference in magnitude between the decelerating part, at the region of the driver, $E_z^b = E_z(\zeta_b)$, and the accelerating part, at the rear of the blowout, $E_z^w = E_z(\zeta_w)$ (Figure 1 (b)). The ratio of these two magnitudes is called the transformer ratio

$R_w \equiv |E_z^w/E_z^b|$. The energy gain of a witness electron beam, placed at the rear position of the wake is thus given by $\Delta\gamma_w mc^2 = R_w \gamma_b mc^2$ after energy depletion of an electron driver beam with initial mean Lorentz factor of γ_b . Longitudinally symmetric drivers cannot excite plasma waves with transformer ratios $R_w > 2$ in the linear regime³⁷. However, in the blowout regime, symmetric Gaussian profiles can generate transformer ratios $R_w > 3$ (cf. Figure 1(b)), and triangularly ramped profiles³⁸ can reach even $R_w > 5$. The Wakefield-Induced Ionization (WII) injection method exploits the fact that wakefields in the blowout regime in PWFA have transformer ratios significantly greater than one to induce ionization and trapping of high-quality electron bunches into the extreme accelerating fields of the plasma wake. These electrons originate from an atomic species with high ionization threshold (HIT) which is doped into the background plasma in a short axial region of the plasma target.

The ionization process caused by static (or slowly varying compared to the ionization process) electric fields of a magnitude sufficient to significantly deform the atomic potential barrier can be described by a tunnelling probability³⁹, which has been determined for a number of atomic species⁴⁰. In Figure 2 the ionization probability rates (W_I) are depicted as a function of the total electric field $E \equiv |\mathbf{E}|$, for some different types of gases. These probability rates grow exponentially as soon as E approaches an ionization threshold, which is defined here as the field E_{ion} for which the ionization probability rate becomes $W_I = 0.1 \text{ fs}^{-1}$. According to this definition, the ionization threshold is written in units of GV/m in Figure 2 for the set of selected atomic species.

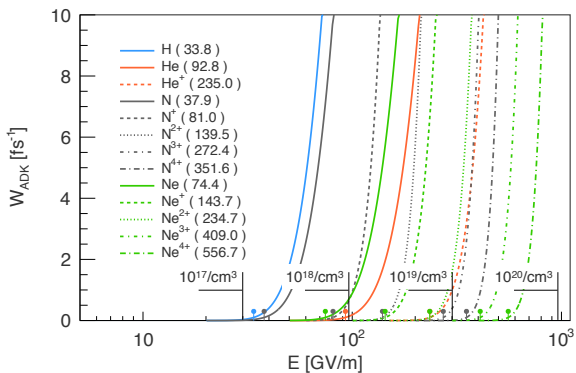


Figure 2. Ionization probability rates according to the theory by Ammosov, Delone, and Krainov (ADK)⁴⁰. The ionization thresholds are indicated by the dots and their numerical values written in units of GV/m. The flags on the x-axis are placed at field values corresponding to E_0 for four different plasma densities.

Generally, the field configuration of the beam driver and wakefield in the blowout regime enables both ionization and trapping from two regions within the first wave bucket²⁵. One region is located at the driver beam position, where the combination of the radial electric field

of the beam driver and the electric wakefield can induce ionization, if sufficiently high. In the following the maximum electric field magnitude in the region of a high current, tightly focused beam driver is computed to estimate the conditions for the onset of ionization in this region. The radial electric field in the blowout can be calculated via Gauss' law, for a given charge density of the drive beam and with the homogeneous ion charge density in the blowout. For axially symmetric Gaussian beams ($n_b = n_b^0 e^{-\zeta^2/2\sigma_z^2 - r^2/2\sigma_r^2}$), the radial electric field is then given by

$$\frac{E_r}{E_0} = -\frac{\Lambda_b}{k_p r} \left(1 - e^{-\frac{r^2}{2\sigma_r^2}}\right) + \left(1 - \frac{\partial_\zeta E_z}{k_p E_0}\right) \frac{k_p r}{2}, \quad (1)$$

where $\Lambda_b(\zeta) = k_p^2 \int_0^\infty \frac{n_b}{n_0} r dr$ is the normalized charge per unit length of the beam. Λ_b is related to the electric current of the beam by $\Lambda_b = (k_p^2/2\pi e c n_0) I_b = 2 I_b/I_A$, where $I_A = 4\pi\epsilon_0 mc^3/e \simeq 17.05 \text{ kA}$ is the Alfvén current. The above defined beam thus has the normalized current profile $\Lambda_b = (n_b^0/n_0) (k_p \sigma_r)^2 e^{-\zeta^2/2\sigma_z^2}$. The first term in Eq. (1) corresponds to the contribution from the beam charge density, while the second term represents the contribution from the uniform charge density of ions plus the slope of the longitudinal wakefield inside the cavity. In the drive beam region, $k_p^{-1} \partial_\zeta E_z/E_0 \ll 1$ and this contribution to the second term in Eq. (1) can be neglected. Furthermore, for high-current ($\Lambda_b \gtrsim 1$), tightly focused ($k_p \sigma_r \lesssim 1$) beams, the first term in this equation dominates over the second term and the maximum of E_r can be obtained analytically from Eq. (1)

$$\frac{E_r^{\text{max}}}{E_0} \simeq -0.45 \frac{\Lambda_b}{k_p \sigma_r}. \quad (2)$$

This maximum value is reached at distance $r \simeq 1.585 \sigma_r$ from the center of the beam's propagation axis. Given this inverse proportionality of E_r^{max} on σ_r , the magnitude of the electric field in this region is highly sensitive to the betatron oscillations of the beam envelope σ_r in the focusing ion-cavity^{41,42} and fluctuations in the slice-emittance and current profile.

The second region from which ionization and subsequent trapping can occur is located at the rear of the ion-cavity, where only the wakefields induce ionization. While the electric field magnitude in the beam region depends on details of the beam's charge distribution, the electric wakefield behind the driver, in the back of the cavity, does not depend on these details, but only on the geometrical structure of the blowout. An important feature of the blowout regime may be noted in this regard: The structure of the plasma wake is mainly sensitive to the integrated charge per unit length of the driver, and not to its transverse distribution, as long as the envelope of the drive beam is sufficiently smaller than the blowout radius $\sigma_r \ll r_l$. This can be seen in Eq. (1), where the impact of the electric field on the plasma electrons in the sheath for $r = r_l \gg \sigma_r$ is dominated by the normalized current profile of the drive beam Λ_b . This

implies that the wakefields are not sensitive to betatron oscillations and fluctuations of the driver beam distribution, and remain stable. The WII injection exploits this fact to induce ionization by means of the wakefields only, while avoiding any contribution from the electric fields in the driver's region. For this reason, the dopant species has to be chosen to have an ionization field threshold above the maximum value in the driver's region E^b , and smaller than the electric field magnitude at the back of the cavity E^w . For high-current, moderately wide beams, i.e. $k_p\sigma_r \approx 1$, and $\sigma_r < r_l$, the radial electric beam field is significantly smaller than the longitudinal magnitude of the wakefield in regions near the propagation axis. Given the absence of any current, also the magnitude of the electric field in the back of the cavity behind the drive beam can be approximated by the longitudinal component only. The condition for ionization to occur only in the rear part of the cavity might hence be written as

$$|E_z^w| > E_{\text{ion}} > |E_z^b|, \quad (3)$$

with E_{ion} the ionization threshold of the given HIT species. In order to complete the injection, ionization must be followed by trapping of the released electrons. Electrons are only trapped if they do not escape the focussing channel of the blowout while gaining a sufficiently large velocity to co-propagate with the plasma wake at $v_b \approx c$. Considering that the electrons are released at rest in a phase position ζ_i , the velocity of the ultrarelativistic wake can be only acquired if the electrons end up in a phase position ζ_f that satisfies

$$\Delta\psi \equiv \psi_i - \psi_f = 1, \quad (4)$$

where ψ is the normalized wake potential, related to the wakefields by $E_z/E_0 = -\partial_\zeta\psi/k_p$ and $W_\perp/E_0 = -\partial_r\psi/k_p$. Eq. (4) is a necessary but not sufficient condition for trapping, which is obtained from the constant of motion of electrons²⁴ under the quasi-static approximation⁴³. Thus, in order to allow trapping from ionization, the plasma wake must provide a minimum difference in normalized wake potential of $\Delta\psi = 1$. Figure 1 (e) shows the structure of ψ in the central slice of the example simulation. The maximum potential ψ_m is reached at the center of the blowout cavity (ζ_m), where E_z changes from positive to negative and the cavity radius is maximal ($r_l = r_m$). The minimum ψ_{min} is located at the very end of the cavity, ζ_c , where the plasma electrons cross the propagation axis and E_z changes from negative to positive values (cf. Figure 1(e)). The maximum potential difference of ψ is therefore given by the integral $\Delta\psi_{\text{max}} = -k_p \int_{\zeta_m}^{\zeta_c} (E_z/E_0) d\zeta$. The phenomenological models for the blowout regime^{31,32} connect E_z with the dynamics of the plasma electrons in the plasma sheath. A particularly clear differential equation for E_z is provided in³¹,

$$\frac{\partial_\zeta E_z}{k_p E_0} = -\frac{2\Lambda_b}{(k_p r_l)^2} + \frac{4}{(k_p r_l)^2} \left[\frac{E_z}{E_0} \right]^2 - \frac{\beta_{lz}}{1 - \beta_{lz}}. \quad (5)$$

Eq. (5) explicitly expresses the dependence of $\partial_\zeta E_z$ on the cavity radius r_l , the magnitude of E_z itself, and finally, the longitudinal velocity β_{lz} of the plasma electrons in the screening layer, and it is used for estimations in the context of this paper. For sufficiently high-current Gaussian beams ending before the cavity center, this model (Eq. (5)) connects both the maximum decelerating field in the region of the drive beam, $E_z^b = E_z(\zeta_b)$, and the maximum blowout radius, r_m , with the peak current of the drive beam, Λ_b^0 ,

$$E_z^b/E_0 \approx \sqrt{\Lambda_b^0/2}, \quad (6a)$$

$$(k_p r_m)^2 \approx \sqrt{32\pi\Lambda_b^0} (k_p \sigma_z). \quad (6b)$$

In addition, it can be seen that, in case of a large blowout radius $k_p r_m \gg 1$, the electrons in the plasma sheath acquire high speed in backwards direction in respect to the driver beam propagation. If the beam has a negligible current at the region of maximum radius within the blowout, one finds from Eq. (5) that E_z is proportional to ζ in a wide region from the cavity center towards the back. The slope of the longitudinal field is defined entirely by the plasma sheath velocity

$$\frac{\partial_\zeta E_z}{k_p E_0} = -\frac{\beta_{lz}}{1 - \beta_{lz}} \approx \frac{1}{2}, \quad (7)$$

where the last approximation is obtained in the limit of $\beta_{lz} \rightarrow -1$. Under the assumption that E_z continues with this linear slope from ζ_m up to the end of the cavity ζ_c , it is possible to find a simple estimate for the magnitude of E_z^w , and the maximum difference in wake potential

$$E_z^w/E_0 \approx \frac{k_p l_m}{2}, \quad (8a)$$

$$\Delta\psi_{\text{max}} \approx \left(\frac{k_p l_m}{2} \right)^2, \quad (8b)$$

where $l_m \equiv \zeta_m - \zeta_c$ is defined as the longitudinal semi-axis of the ion-cavity (Figure 1 (a)).

In this work, we compare these approximate scalings with results from 3D simulations obtained with the PIC code OSIRIS. The series of simulations consists on axially symmetric Gaussian beams of fixed geometrical dimensions ($k_p\sigma_z = \sqrt{2}$ and $k_p\sigma_r = 0.1$), fixed normalized emittance ($k_p\epsilon_n = 0.31$) and variable peak current I_b^0 , ranging from 1 kA up to 60 kA. Figure 3(a) shows r_m (black line) and l_m (grey line) as a function of the peak current of the beam. The top dashed line is the blowout radius obtained from Eq. (6b) for $k_p\sigma_z = \sqrt{2}$, i.e. $8\sqrt{\pi\Lambda_b^0}$. It is worth noting that, despite the fact that this radius overestimates r_m for relatively low currents, it reproduces the scaling of l_m . The second dotted line is defined by

$$k_p r_m \approx 2\sqrt{\Lambda_b^0}, \quad (9)$$

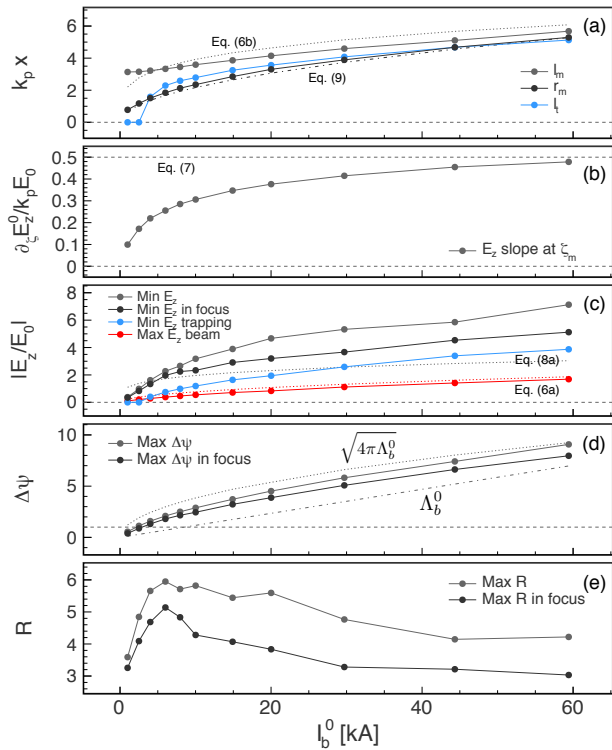


Figure 3. Scaling of key parameters in the blowout regime of PWFA as a function of the peak current of Gaussian drive beams. (a) Transverse (r_m) and longitudinal (l_m) semi-axis of the ion cavity plus the semi-axis of the trapping zone (l_t). (b) Derivative of E_z with respect to ζ at the cavity center. (c) Magnitude of the maximum E_z at the back end of the cavity (grey line), inside the focusing region (black line), in the trapping zone (blue line) and in the driver region (red line). (d) Maximum wake potential difference in the blowout cavity (grey line) and in the focusing region (black line). (e) Maximum transformer ratio in the cavity (grey line) and in the focusing region (black line). The dotted lines represent certain model estimations that are explained on the text.

which is a well known scaling of the transverse blowout radius as a function of the driver current, for moderate length Gaussian drivers ($k_p \sigma_z \approx \sqrt{2}$), obtained from PIC simulations^{32,41}. For high peak currents, r_m obtained from Eq. (9) as well as r_m obtained from Eq. (6b) asymptotically converge towards l_m in the PIC simulations. The sheath of plasma electrons hence approximately follows a spherical shape behind the driver beam for high current drivers. The scaling for the blowout radius with the beam peak current in Eq. (6b) in this comparison is identified as an accurate estimation for l_m (cf. Figure 3(a)). Hence, the maximum ψ difference may be connected with the current of the driver beam $\Delta\psi_{\max} \approx \sqrt{4\pi\Lambda_b^0}$, by means of this scaling. In contrast, the scaling for r_m from Eq. (9) was used in a previous work²⁵ to express the maximum wake potential difference as a function of the driver's current $\Delta\psi_{\max} \approx \Lambda_b^0$, and

hence, estimate the minimum peak current for Gaussian beams to allow for trapping from ionization: $\Lambda_b^0 > 1$. In Figure 3(d), we show the scaling of $\Delta\psi_{\max}$, as obtained from full 3D PIC simulations (grey line), together with the two estimations above. The dotted line shows $\sqrt{4\pi\Lambda_b^0}$, while the dash-dotted line depicts Λ_b^0 . Although slightly above, the $\sqrt{4\pi\Lambda_b^0}$ scaling seems to give a better description of the scaling of $\Delta\psi_{\max}$ from PIC simulations.

To be trapped and transported, electrons not only need to reach the velocity of the wake, but also must remain in the focusing region of the plasma wave. PIC simulations show that the position where the cavity closes and where ψ is minimum falls in a defocusing region, so that electrons cannot be transported there. The trapped orbits have to lie completely in the focussing region, ahead of the co-moving position ζ_F at which the field configuration changes from focusing to defocusing (Figure 1(c)). The black line in Figure 3(d) shows the maximum potential difference that can be reached inside the focusing region, i.e. $\psi_m - \psi_F$, which is clearly smaller than the absolute $\Delta\psi_{\max}$ (grey line). The maximum accelerating field in the focusing region is given by $E_z^F \equiv E_z(\zeta_F)$ (black line in Figure 3(c)), to be compared with the absolute minimum at the very end of the cavity (grey line). To be trapped exactly at ζ_F , an electron must be ionized at a position $\zeta_I > \zeta_F$, such that $\psi_I - \psi_F = 1$. The set of points fulfilling this condition form a surface that delimits the *trappable zone*. Electrons released (at rest) inside this zone can *potentially* be trapped in the focusing region of the blowout cavity. The blue line in Figure 3(a) shows $l_t \equiv \zeta_m - \zeta_I$ (the *trapping distance*) as a function of I_b^0 , as obtained from the set of PIC simulations. We see that a *trappable zone* ($l_t > 0$) only exists for sufficiently high peak currents $I_b^0 \gtrsim 5$ kA. This defines a lower limit for the peak current of Gaussian drivers to achieve trapping of electrons based on ionization injection techniques in the quasi-static picture. Nevertheless, we would like to point out here that this limit can be lowered if the phase velocity of the wake is reduced when performing the ionization in a plasma density transition. In order to induce ionization in the trappable region by means of the wakefields at the back of the blowout, the magnitude of the accelerating field at ζ_I , $E_z^I \equiv E_z(\zeta_I)$ (blue line in Figure 3(c)) has to be greater than the ionization threshold of the dopant species $|E_z^I| > E_{i\text{on}}$. In addition, it is important to avoid any spurious contribution from the evolving electric fields in the driver's region (cf. Figure 4(b)). As we saw from Eq. (1), the radial electric field is sensitive to the envelope betatron oscillations of the beam, and it increases significantly when the beam envelope is reduced. Electrons ionized by the radial fields in the driver beam region gain transverse momentum while they are still slow ($\ll c$), and are likely to escape the relativistic focusing cavity in the transverse direction. Another reason to avoid ionization in the beam region is the fact that narrow beams can ionize entirely the dopant species around the axis, leaving no atoms or molecules which can be ionized in

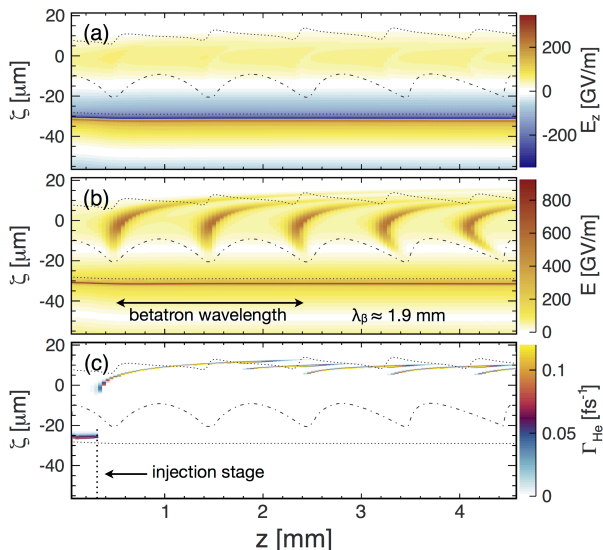


Figure 4. Evolution of the longitudinal electric field (a), the total electric field (b) and the ionization rate from He (c) in the on-axis region, for an unmatched 10 kA Gaussian electron driver. The dotted lines delimit the on-axis phase range with $\psi - \psi_F > 1$. The dotted-dashed lines represent the end of the region where the radial fields of the beam are highly defocusing for slow electrons ($E_r \ll 0$).

the rear wakefields. For these reasons, beams in WII injection should not trigger ionization themselves in regions near the axis. It is interesting to note that the beam spot size that makes E_r^{\max} in Eq. (2) equal to E_z^b in Eq. (6a) is given by $k_p \sigma_r \simeq 0.64 \sqrt{\Lambda_b^0}$, which is always much smaller than the blowout radius in Eq. (9). The latter condition ensures that the total electric field is dominated by its longitudinal component in the beams region near the propagation axis, while maintaining the condition for a stable blowout ($\sigma_r < r_m$). However, unless the beam is matched to the focusing plasma channel, this situation does not last, and the injection must occur before the beam is transversely compressed due to the betatron oscillations within the ion channel. After the injection, it is preferable that the driver beam is tightly focused to ensure a stable propagation that mitigates the head erosion⁴⁴. This sets a condition for the normalized transverse emittance of the beam to be smaller than the matched value $k_p \epsilon_n < \sqrt{\gamma/2} (k_p \sigma_r)^2$. The spatial period of the envelope oscillations of the beam is given by half the betatron wavelength⁴² of the beam-particles in the blowout $\lambda_\beta = \sqrt{2\gamma}/k_p$. Figure 4 shows the evolution of E_z (a) and $E = |\mathbf{E}|$ (b) in the on-axis region ($k_p r < 0.1$), for the Gaussian driver beam in the example of Figure 1. Due to the envelope oscillations of the beam, the total electric field in the driver's region oscillates with a spatial periodicity of $\lambda_\beta/2$ (Figure 4(b)). On the contrary, the longitudinal fields (in Figure 4(a)) are stable during the propagation. After the beam is transversely compressed, the region with a high ionization rate moves from the

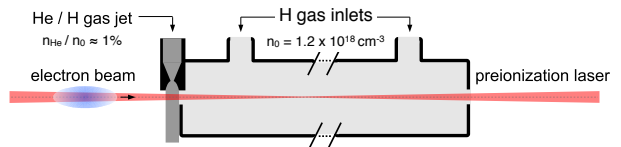


Figure 5. Schematic of the plasma-cell setup assumed as a basis for the OSIRIS 3D simulations. A thin jet of a neutral hydrogen/helium gas mixture upstream of a flat-top hydrogen gas target assures localized WII injection. The hydrogen is pre-ionized with a laser while the helium remains non-ionized.

back of the cavity to the front of the beam (Figure 4(c)).

Figure 3(c) depicts the on-axis values for the longitudinal electric field at the smallest possible co-moving position from which electrons can still be trapped $E_z^I = E_z(\zeta_I)$ (blue line) and the maximum longitudinal electric field in the beam region E_z^b (red line). The longitudinal electric field in the beam region according to Eq. (6a) is represented by the red dotted line, and closely follows the curve from the simulation data. The grey dotted line in Figure 3(c) is the result of extrapolating the linear tendency of E_z at the cavity center (Eq. (7)) up to the end of the cavity ζ_c . PIC simulations show that the difference in magnitude between E_z^I and E_z^b grows with increasing peak current of the driver, hence allowing a wider range of ionization thresholds for which the ionization in the beam region is suppressed but for which the ionization and trapping in the blowout is still possible. The appropriate dopant species for WII injection must have an ionization threshold $|E_z^I| > E_{\text{ion}} > |E_z^b|$ (blue and red lines in Figure 3(c)). Such an ionization threshold can only be obtained using high-current beams $I_b^0 \gtrsim 8.5$ kA. The criterion for the current corresponds to a normalized current of $\Lambda_b^0 \simeq 1$, and is independent of the plasma density. In addition, Figure 3(b) depicts the slope of E_z around the cavity center (grey line), which converges to the value suggested by Eq. (7) for high-current drivers. Figure 3(e) shows the overall maximum transformer ratio (grey line) and the maximum transformer ratio for witness beams placed within the focusing region (black line) in the PIC simulations.

The theoretical framework for WII injection described above is independent of the choice for the plasma density. However, the choice of a specific plasma density with a specific E_0 requires the choice of an appropriate dopant species with suitable ionization threshold(s) (Figure 2). Ideally, the plasma density is chosen such that the drive beam generates wakefields with the greatest possible transformer ratio. This is the case at the so-called resonant length, which in the linear regime⁴⁵ is given by $k_p \sigma_z = \sqrt{2}$. The horizontal lines in Figure 1(d) indicate the ionization thresholds for H, He, and Ne in case of $E_0 = 105$ GV/m, which corresponds to a plasma density of $n_0 = 1.2 \times 10^{18} \text{ cm}^{-3}$. For this particular example, the first ionization thresholds of He and Ne (solid or-

ange and green lines in Figure 1(d), respectively) fulfil the condition expressed in Eq. (3) and can be used for WII injection.

In order to exemplify and further analyze the characteristics of WII injection and the trapped bunches, results from PIC simulations on two experimental setups will be presented in the following. These are the FLASHForward project at DESY and the FACET facility at SLAC. The experimental setup considered is sketched in Figure 5; The plasma is pre-created by a laser pulse with an intensity sufficiently high to fully ionize a gas with a low ionization threshold (LIT), e.g. hydrogen along the propagation axis of the drive beam. In addition, a micro-nozzle⁴⁶ fed by the same LIT gas doped with a tunable concentration of a high-ionization-threshold (HIT) gas (e.g. helium), is positioned in the vicinity of the gas-cell entrance. Because the electrons to be injected in the wake by means of Wakefield-Induced Ionization will originate from the HIT dopant gas, it must remain non-ionized after the passage of the ionization laser and the electron driver beam. This technology for the plasma cell⁴⁷ also allows the density profile of the gas components to be controlled by means of several gas inlets with tunable pressure. The density profile configuration for WII injection can be simple and we only consider the case in which the density of the LIT gas is approximately uniform all along the main channel and the micro-nozzle. The doped gas jet emerging from the nozzle can spatially be confined to a distance which is significantly shorter than the betatron wavelength, so that an unmatched beam experiences maximum transverse compression downstream of the doped gas nozzle.

III. FLASHFORWARD AT DESY

FLASHForward (Future-oriented wakefield-accelerator research and development at FLASH) is a plasma-wakefield acceleration project at DESY, which utilizes high current and short electron beams from the versatile FLASH accelerator. The standard operational mode of the FLASH accelerator offers electron bunches with approximately Gaussian longitudinal ($\sigma_z \sim 20 \mu\text{m}$) and radial ($\sigma_r = 10 \mu\text{m}$) profiles, transverse normalized emittances of $\epsilon_n \approx 1 \mu\text{m}$, and an energy of 1 GeV with a relative spread of 0.1 %. Such bunches are to be compressed even further in the beam-extraction arc upstream of the FLASHForward plasma cell, to reach peak currents of up to $I_b \approx 10 \text{ kA}$ in a more compact size ($\sigma_z \sim 7 \mu\text{m}$ and $\sigma_r = 4 \mu\text{m}$). Operating this current-enhanced FLASH-Forward driver at the resonant length ($k_p \sigma_z = \sqrt{2}$) requires a plasma density of $n_0 = 1.2 \times 10^{18} \text{ cm}^{-3}$. This results in parameters for the electron driver and the density that correspond to the parameters used for the PIC simulation in Figure 1 for a 10 kA Gaussian driver. As pointed out at the end of Sec. II, at this plasma density the first ionization levels of both He and Ne match the condition for WII injection (Eq. (3)) with a 10 kA beam.

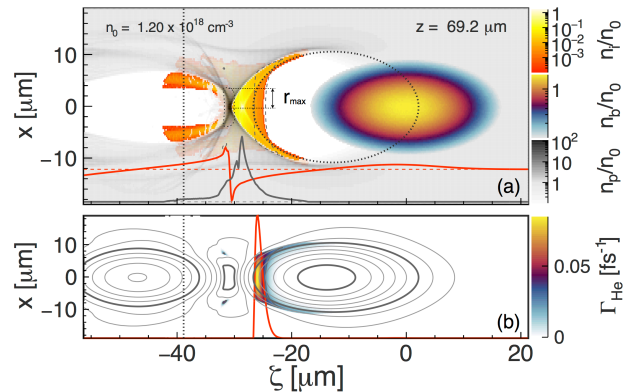


Figure 6. OSIRIS 3D simulation of a FLASHForward-type electron beam ($I_b = 10 \text{ kA}$), traversing a plasma at the resonant density ($n_0 = 1.2 \times 10^{18} \text{ cm}^{-3}$). (a) Spatial particle density. (b) Ionization rate for He according to the ADK model. The contours in panel (b) show profiles of the equipotential surfaces. These surfaces are depicted in steps of 0.2 starting from the minimum value inside the focusing region (ψ_F). The vertical dotted line indicates the beginning of the He region.

Figure 6(a) shows a snapshot of the simulation when the beam traverses a $L_{\text{He}} = 60 \mu\text{m}$ diameter gas-jet doped with He at $n_{\text{He}} = 0.01 n_0$ concentration. Figure 6(b) shows the expected ionization rate from the outer He electron in a configuration with a 10 kA peak current beam operating in a plasma of $n_0 = 1.2 \times 10^{18} \text{ cm}^{-3}$. Because the gas streams from right to left at c in this co-moving picture, the ionization rate is computed taking into account the He electrons that have been already ionized

$$\Gamma_I(\zeta) \equiv W_I(\zeta)(1 - P_I(\zeta)), \quad (10)$$

where $W_I(\zeta) = W_I(E(\zeta))$, the species ionization rate according to the ADK model⁴⁰ and

$$P_I(\zeta) \equiv c^{-1} \int_{\infty}^{\zeta} W_I(\zeta') d\zeta', \quad (11)$$

the ionization probability in the co-moving frame. The regions with a high ionization rate will be denoted as the *ionization volume*. The volume from which injection is possible is thus determined by the intersection of the ionization volume ($E > E_{\text{ion}}$) with the volume satisfying the trapping criterion ($\psi - \psi_F > 1$). The contours of $\psi - \psi_F$ are drawn in Figure 6(b), showing that only a narrow and well-defined region around the propagation axis satisfies the conditions for simultaneous ionization and trapping. Owing to the small size of this injection volume, the trapped orbits will also be confined in a small transverse region and short phase interval during the acceleration process. These are prerequisites for the generation of intrinsically very short and low-emittance electron bunches. The ionization rate increases quickly as

soon as the wakefield exceeds the ionization threshold, thereby defining a narrow spike of high ionization rate in the on-axis region (red line in Figure 6(b)). Electrons originating from this location ζ_i are trapped at ζ_f complying with $\psi(\zeta_i) - \psi(\zeta_f) = 1$. Because the ψ contours are closer to each other when the electrons approach the trapped positions, the longitudinal distribution during the acceleration of the injected electron bunch is narrower than the initial distribution. In the considered example, the rms of the initial ionization volume is significantly smaller than the plasma skin depth k_p^{-1} . Due to the invariance of E_z along the cavity radius, the volume of injection extends transversely up to r_l . Furthermore, the radial electric field increases linearly with increasing radius (Eq. (1)) and thus, the ionization rate is greater in positions close to the transverse boundary of the cavity. However, electrons ionized close to the boundary are, either out of the trapping region or escape transversely due to sizeable transverse momentum gain from the positive transverse electric field in the most off-axis regions. The initial injection volume may therefore be considered as a thin disc centred on axis which extends up to a radial position r_{\max} that is always smaller than the cavity radius at that point (cf. Figure 6(a)). The finally injected witness bunch is composed of electrons ionized from within this volume. Electrons belonging to the same final ζ_f slice originate from different radial positions along the initial ψ_i contour. Assuming full betatron decoherence for every slice, an upper estimate of the normalized transverse emittance can be given in terms of the initial transverse extent of the slice²⁵ $\epsilon_n = k_p \langle r_i^2 \rangle / 4$. Considering for simplicity, the ionization electrons to be uniformly distributed up to r_{\max} along the largest ψ_i contour, the estimated maximum slice emittance yields

$$k_p \epsilon_n^{\max} = \frac{(k_p r_{\max})^2}{12}. \quad (12)$$

Typically r_{\max} is much smaller than the maximum blowout radius r_m provided that ionization and trapping only happens from the core of a thin ionization slice at a rear position of the blowout cavity. For this reason, the WII injected bunches are, by construction, extremely compact and low emittance. As a very practical rule of thumb, we can write the following relation for the WII injected bunches

$$k_p \sigma_z \sim k_p \epsilon_n \sim 0.1. \quad (13)$$

That is, both the length and the normalized emittance of the injected bunch are a fraction of the plasma skin depth, which scales with the inverse of the squared root of the plasma density ($k_p^{-1} \propto 1/\sqrt{n_0}$).

Figure 7 shows the density of the driver-witness system after 14.6 mm of propagation in plasma in the simulation discussed above, where a short (240 nm) bunch of electrons has been ionized and injected from the neutral He by means of the wakefields only. The total injected charge amounts to 6.43 pC, while the rms current, defined as

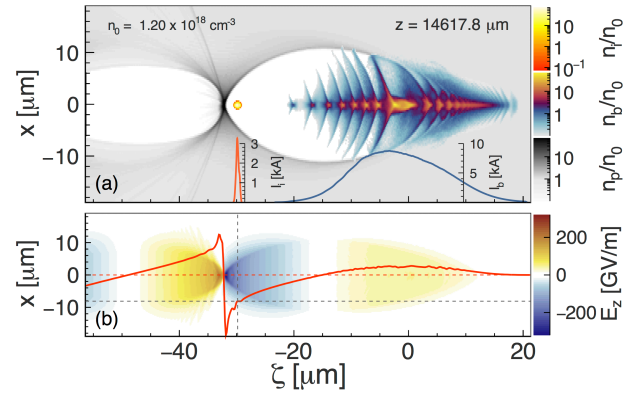


Figure 7. Results from the same PIC simulation as in Figure 6, but after 14.6 mm of propagation in plasma. (a) Spatial particle density. Here a short bunch of 6.34 pC has been injected and subsequently accelerated up to more than 2.5 GeV energy. (b) Longitudinal electric fields. The bunch experiences an accelerating gradient substantially greater than 100 GV/m.

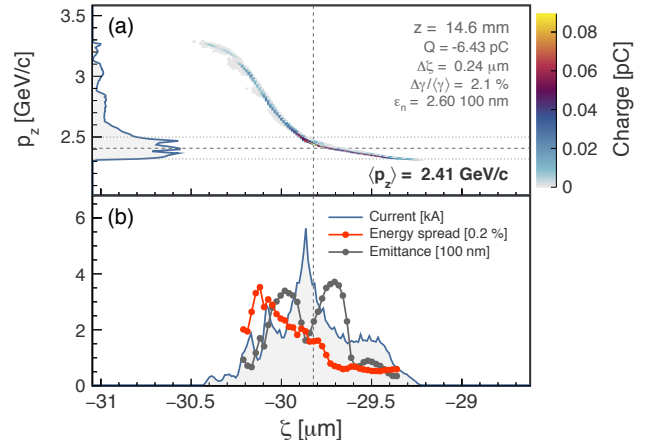


Figure 8. Witness bunch properties after 14.6 mm of acceleration. (a) Absolute charge distribution of the bunch in longitudinal phase space (p_z vs. ζ plane). The projection of this distribution in p_z is depicted on the left axis. (b) Bunch-current profile. The relative energy spread and the transverse emittance are plotted for different longitudinal slices along the bunch.

$I_{\text{rms}} = cQ/(\sqrt{2\pi}\sigma_z)$, is equal to 3.2 kA. Note that with this definition, the peak and rms currents for Gaussian beams are identical. The injected beam has been accelerated over a distance of 14.6 mm, from $\langle \zeta_f \rangle \approx -29.8 \mu\text{m}$, where $E_z(\langle \zeta_f \rangle) \approx 136 \text{ GV/m}$ (Figure 7(b)).

Some additional properties of the trapped bunch can be estimated from the initial phase-space distribution as well. Trapped electrons with the same initial ψ_i propagate to the same final position ζ_f , which fulfils $\psi_i - \psi_f = 1$; they will be accelerated by the same field value $E_{z,f}$. However, each one of these slices in

ζ_f is composed of electrons ionized at different longitudinal positions along the He column, and therefore are accelerated over different times, producing a finite spread in longitudinal momentum in every slice given by $\Delta p_{z,f} \simeq -eE_{z,f} L_{\text{He}}$, which at the average position of the bunch gives $\Delta p_{z,f} \approx 8 \text{ MeV}/c$. This is identified as the main contribution to the sliced energy spread of the beam, as other sources of thermal spread (e.g. helium temperature) on the initial population of injected electrons are considered to be well below MeV levels. Because this initial sliced energy spread due to the finite width of the dopant jet is not expected to grow during the acceleration process, the sliced relative energy spread of the bunch $\Delta\gamma_f/\langle\gamma_f\rangle = \Delta p_{z,f}/\langle\gamma_f\rangle mc$ can reach values well below 1% at 1 GeV electron energies. On the other hand, the total relative energy spread is proportional to the variation of E_z along the bunch, which in case of negligible beam loading and sufficiently short bunches is approximately given by $\Delta\gamma/\langle\gamma\rangle \simeq (\partial_\zeta E_{z,f}/E_{z,f}) \sigma_{z,f}$. This quantity does not depend either on the beam's electron energy or on the plasma density, but only on the product of the local E_z slope and its length. Using Eq. (7) to approximate the magnitude of the E_z slope, and Eq. (12) for the bunch size, $\Delta\gamma/\langle\gamma\rangle \approx 5\%$ for WII injected witness bunches. From Figure 7(b), $\partial_\zeta E_z(\langle\zeta_f\rangle) \approx 28.9 \text{ (GV/m)} \mu\text{m}^{-1}$, and $\Delta\gamma/\langle\gamma\rangle \approx 8.8\%$.

The properties of the simulated injected bunch after acceleration over a distance of 14.6 mm are summarized in Figure 8. The longitudinal phase space (Figure 8(a)) exhibits a thin curved chirp with an average energy of $\sim 2.55 \text{ GeV}$ and a projected relative energy spread of 8.8%. The horizontal dotted lines in Figure 8(a) delimit the full width at half maximum (FWHM) for the projected energy spectrum on the left. The value of relative energy spread ($\sim 2\%$) in FWHM is given in the figure. Additional bunch properties can be seen in more detail in Figure 8(b). The current profile has a maximum approximately at the center of the bunch of $\sim 5 \text{ kA}$. The relative energy spread ($\lesssim 0.3\%$), and the normalized transverse emittance ($\lesssim 300 \text{ nm}$) are shown for different slices in ζ . The slice width (0.005 k_p^{-1}) is chosen short enough such that a further reduction of this width would not significantly change the values of the sliced properties, in order to appropriately reflect their uncorrelated values. The maximum uncorrelated normalized emittance along the bunch is $k_p \epsilon_n^{\text{max}} = 0.06$, which may be connected with the injection volume maximal radius as discussed above. Knowing the emittance in the simulation, the maximum ionization radius can be estimated by using Eq. (12), $r_{\text{max}} \approx 0.86 \text{ k}_p^{-1} = 4.2 \mu\text{m}$, which matches well with the simulations (cf. Figure 6(a)).

IV. FACET AT SLAC

The next example considers electron bunches similar to those provided by FACET at SLAC. These beams²⁶ can be approximated by Gaussian longitudinal ($\sigma_z = 14 \mu\text{m}$)

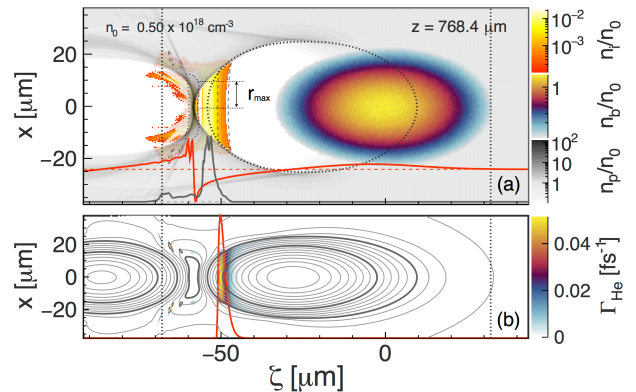


Figure 9. OSIRIS 3D simulation of a FACET electron beam ($I_b = 23 \text{ kA}$), traversing a plasma with $n_0 = 0.5 \times 10^{18} \text{ cm}^{-3}$ and resonantly exciting a plasma wave. (a) Spatial particle density. (b) Ionization rate map for He according with the ADK model. The contours in panel (b) outline the isopotential regions. They are drawn in steps of 0.2 starting from the minimum value inside the focusing region (ψ_F). The vertical dotted line indicates the beginning of the He region.

and transverse ($\sigma_x = \sigma_y = 10 \mu\text{m}$) profiles with peak currents of 23 kA, transverse normalized emittances of $\epsilon_{n,x} = 50 \mu\text{m}$ and $\epsilon_{n,y} = 5 \mu\text{m}$, and an energy of 23 GeV with a relative spread of 1%. The most important difference with respect to the FLASHForward case in Sec. III is the significantly higher peak current of the driver beam $\Lambda_b^0 = 2.7$. Figure 9 shows a simulation of the FACET beam transversing a $n_0 = 5 \times 10^{17} \text{ cm}^{-3}$ density plasma doped with He at $n_{\text{He}} = 0.002 n_0$, within a gas jet of $L_{\text{He}} = 100 \mu\text{m}$ diameter. The fact that the blowout is bigger in this case, implies that the maximum difference of the wake potential $\Delta\psi_{\text{max}}$ is bigger in the focusing region of the ion cavity (cf. Figure 3). This allows for more flexibility for the selection of the HIT species, provided that the difference between E_z^1 and E_z^b is equivalently greater. This also means that the HIT species can be chosen in a way that ionization happens closer to the end of the cavity, where the blowout radius gets smaller so that the injection volume is more uniform and constrained. Figure 9(b) shows the ionization volume within the FACET beam blowout, on top of the wake potential contours. Here, the ionization volume is basically a part of the trapping region, but, as discussed before, the electrons with large initial offsets with respect to the axis escape the blowout region. A sufficient condition for trapping of an electron is that it reaches a ψ_f contour before escaping the blowout in straight backward propagation. The maximum radius fulfilling this specific condition is $r_{\text{max}} \approx 1.6 \text{ k}_p^{-1} = 12 \mu\text{m}$ (cf. Figure 9(b)). This allows the volume of injection to be estimated $V_{\text{inj}} \simeq \pi r_{\text{max}}^2 \Delta\zeta_{\text{ion}}$ and hence of the total trapped charge $Q_{\text{He}} \simeq -en_{\text{He}} \pi r_{\text{max}}^2 L_{\text{He}} = 7.2 \text{ pC}$. Figure 10 shows a short bunch of $0.8 \mu\text{m}$ (rms) length and 8.77 pC charge, propagating with an accelerating

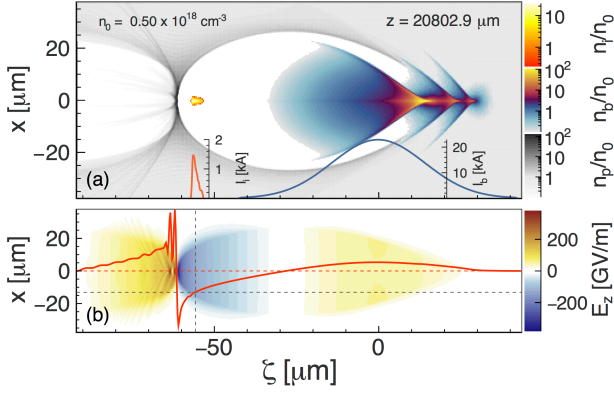


Figure 10. Same simulation as in Figure 9, but after a distance of 20.8 mm of propagation in plasma. (a) Spatial particle density. Here a short bunch of 8.77 pC has been injected and subsequently accelerated up to more than 2.5 GeV energy. (b) Longitudinal electric fields. The bunch experiences an accelerating gradient largely beyond 100 GV/m.

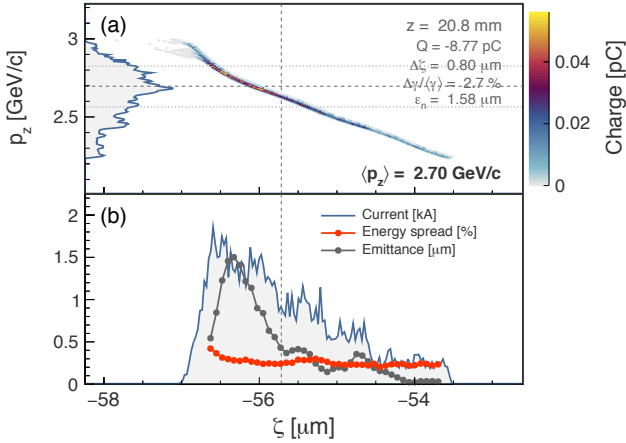


Figure 11. Witness bunch properties after 20.8 mm of acceleration. (a) shows the absolute charge distribution of the bunch in longitudinal phase space (p_z vs. ζ plane). The projection of this distribution in p_z is depicted on the left axis. (b) displays the bunch-current dependence on ζ . The relative energy spread and the transverse emittance are plotted for different longitudinal slices along the bunch.

field of $E_z \approx 130$ GV/m (Figure 10(b)). At this point the injected bunch has been propagating for 20.8 mm in the plasma wake. The bunch properties are shown in Figure 11 in more detail. The longitudinal phase space (Figure 11(a)) exhibits a linear chirp with an average energy of ~ 2.6 GeV, a total relative energy spread of 6% and a relative energy spread in FWHM of 2.7%. The sliced bunch properties can be seen in more detail in Figure 11(b). The current profile has a maximum at the tail of the bunch of ~ 1.5 kA and linearly decays towards its front (Figure 11(b)). The relative energy spread ($\sim 0.3\%$), and the normalized transverse emit-

tance ($\leq 1.5 \mu\text{m}$) are shown for different slices in ζ . Considering $r_{\text{max}} = 12 \mu\text{m}$ and Eq. (12), the estimated normalized emittance is $1.4 \mu\text{m}$, in excellent agreement with the simulation. Further acceleration of the captured beam is possible until the driver is energy-depleted. A simple estimate yields the maximum achievable bunch energy when considering the decelerating gradients experienced by the driver beam of 50 GV/m (cf. Figure 10(b)). This limits the driver propagation distance to ~ 46 cm, and hence, the maximum energy of the injected beam to about 46 GeV assuming an acceleration of the trailing bunch at a continuing rate of 100 GV/m.

V. BEAM LOADING

Ionization-based injection methods have the ability of tuning the amount of injected charge by means of the dopant species concentration and/or the length of the injection section (approximately the gas-jet diameter in the here considered case). In the two previous examples the charge of the injected beam was chosen to be low, so that the beam barely deforms the wakefields, and the energy chirp basically is dominated by the local shape of the unloaded wakefield E_z . In general, an electron beam injected in the accelerating region of the blowout cavity deforms the slope of the longitudinal field with respect to the unloaded case. For a given witness-beam current profile Λ_w , this effect can be calculated from Eq. (5). In this discussion, we assume that the bunch is trapped close to, but before the end of the cavity.

As discussed in Sec. II for high-current driver beams, the velocity of the electrons in the plasma sheath approaches the speed of light in the backwards direction ($\beta_{lz} \approx -c$) when electrons in the sheath reach the point of maximal blowout radius. From this point on, the plasma electrons in the sheath are accelerated in the forward direction and the velocity (third) term in Eq. (5) only dominates at the very end of the bubble, when the electrons velocity approaches the speed of light in the right direction ($\beta_{lz} \approx c$). In the following discussion, the sheath velocity term in Eq. (5) was implicitly neglected, considering that the driver bunch is situated at a point where the electrons in the plasma sheath do not have a sufficiently high positive longitudinal velocity to contribute significantly. With this approximation Eq. (5) reads

$$\frac{\partial_\zeta E_z}{k_p E_0} = -\frac{2\Lambda_w}{(k_p r_l)^2} + \frac{4}{(k_p r_l)^2} \left[\frac{E_z}{E_0} \right]^2. \quad (14)$$

This equation allows the current needed to flatten the slope of E_z along the beam to be estimated. Assuming perfect flattening, e.g. the left hand side of Eq. (14) to be identically zero gives

$$\Lambda_w = 2 \left[\frac{E_z^w}{E_0} \right]^2, \quad (15)$$

where Λ_w refers to the normalized charge per unit length of the witness bunch, and E_z^w is E_z at the position of

the witness bunch ζ_w . This is a local criterion on the slope of E_z . The shape of E_z along the bunch is obtained through integration of Eq. (14). This has been done by M. Tzoufras et al.⁴⁸ for certain bunch-current profiles that permit for an analytical solution. Of particular interest are bunch profiles that totally flatten the field slope along the bunch. These are found to be trapezoidal profiles with the maximum located at the leading edge of the beam at ζ_w , linearly decaying towards the tail

$$\Lambda_w = \sqrt{\left[\frac{E_z^w}{E_0}\right]^4 + \left[\frac{k_p r_m}{2}\right]^4} - \frac{E_z^w}{E_0} k_p (\zeta - \zeta_w). \quad (16)$$

Generally, the witness bunches generated by WII injection do not have this ideal trapezoidal shape for an optimally tailored beam loading. In the following we explored how the energy chirp of the witness bunch changes in respect to the unload case in Fig. 11, when the injected charge is increased. Figure 12, presents the parameters of injected bunches for a series of simulations identical other than the concentration of the dopant He in the gas-jet. The simulation results show witness beam pa-

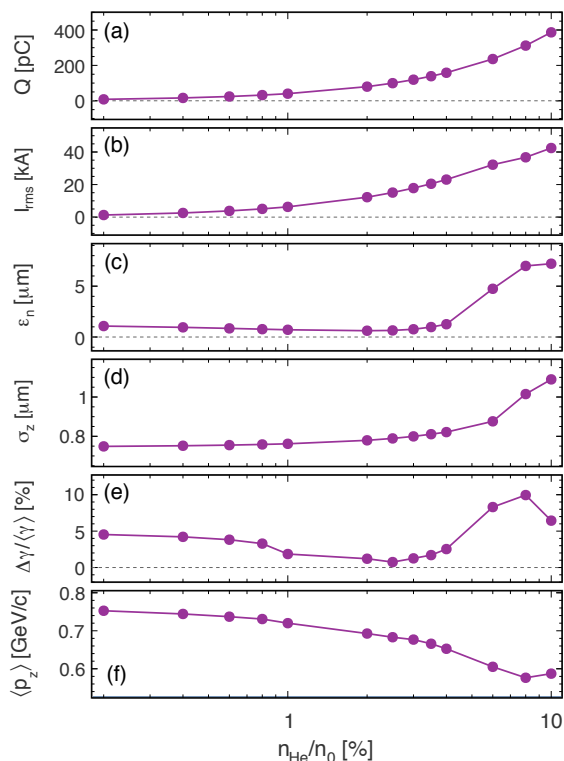


Figure 12. Injected bunch properties after a distance of 5.8 mm of acceleration as a function of the dopant He concentration. (a) Total charge. (b) Current (rms). (c) Normalized emittance. (d) Length (rms). (e) Relative energy spread (FWHM). (f) Average longitudinal momentum.

rameters at a distance of 5.8 mm downstream of the location of the injection. This is substantially before energy depletion of the driving beam occurs, and the energy gain of the witness beam is therefore limited to about 600 – 750 MeV. The data for the lowest He density, $n_{\text{He}} = 0.002 n_0 = 10^{15} \text{ cm}^{-3}$, in Figure 12 corresponds to the bunch obtained in the simulation presented in Sec. IV. As the concentration of He is increased, both the total charge and the rms current of the bunch increase accordingly (see Figure 12(a) and (b)). In contrast, the normalized emittance ϵ_n (Figure 12(c)) and the rms bunch length σ_z (Figure 12(d)) are not changed significantly for increasing bunch charge. This results from both the normalized emittance and the rms length of the injected bunch depending primarily on the volume of injection, so that increasing the He concentration does not have a severe impact. On the contrary, the projected energy spread of the bunch in full width at FWHM (Figure 11) is dominated by the slope of E_z along the bunch, which in turn depends on the current profile of the injected beam (Eq. (14)). Therefore, a clear reduction of the projected FWHM energy spread can be observed (see Figure 12(e)) for increasing charge of the injected bunch. The energy spread is minimal for a dopant density of about $n_{\text{He}} = 0.025 n_0$ (cf. Figure 12(e)). For this case, the injected bunch has a total charge of 100 pC, and a rms current of $I_{\text{rms}} \approx 15 \text{ kA}$ (Figure 13(d)). Both the bunch length $\sigma_z = 0.8 \mu\text{m}$ and the normalized emittance $\epsilon_n = 1.3 \mu\text{m}$ remain at the same magnitude as in the unloaded case. If further increased, the charge of the bunch starts to overload and severely deform the E_z slope. Figure 13 shows the energy chirp for the unloaded case with $n_{\text{He}}/n_0 = 0.2 \%$ (Figure 13(a)), a partially loaded one with $n_{\text{He}}/n_0 = 1.0 \%$ (Figure 13(b)) and the best loaded case with $n_{\text{He}}/n_0 = 2.5 \%$ (Figure 13(c)). More details on the current profile, the sliced energy spread and normalized emittance can be seen in Figure 13(d), for the optimum beam loading case. The peaked projected energy spectrum in Figure 13(c) has a relative energy spread (in FWHM) of only 0.7 %, while in the unloaded case of Figure 13(a), the same quantity amounts up to 4.5 %. This means a reduction of $\sim 85\%$ for optimal beam loading in respect to the unloaded case. The longitudinal phase space correlation is small for the high-current part of the beam, which is accelerated approximately at a constant rate along the intra-bunch axis $E_z^w \approx 117 \text{ GV/m}$.

We compare this result with the theoretical estimations given in Eq. (15) and Eq. (16). Using $E_z^w \approx 117 \text{ GV/m}$ in Eq. (15) leads to a beam current of $I_w \approx 50 \text{ kA}$, while using Eq. (16) with $k_p r_m = 3.3$ (Eq. (9)), one obtains $I_w \approx 34 \text{ kA}$. The current profile of the bunch in the PIC simulation (Figure 13(d)) has peak currents on the order of 30 kA, which is not far from these analytical estimations. Based on these results, and on the applicability of the scalings for $k_p r_m$ and E_z^b (Eqs. (9) and (6a)) with the peak current of the drive beam, we find the following expression relating the peak current of the witness and the driver beam with the actual driver-to-witness energy

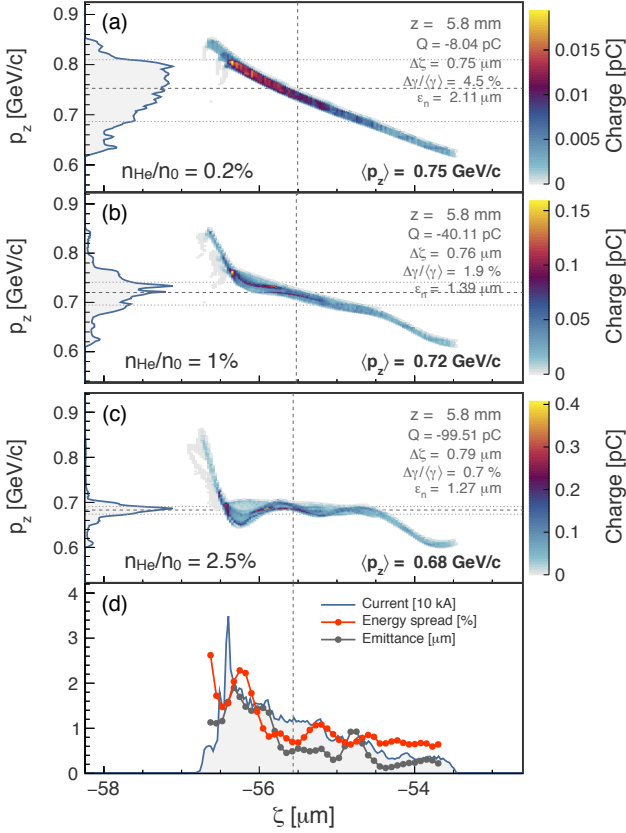


Figure 13. Longitudinal phasespace of the witness bunches after acceleration over a distance of 5.8 mm, for the unloaded case (a), a partially loaded one (b) and the optimized beam loading case (c). The projection of these distribution in p_z are depicted on the left axis. The bunch-current profile, the relative energy spread and the transverse emittance are plotted in panel (d) for various longitudinal slices along the optimized bunch.

transformer ratio R_w

$$\frac{I_w}{I_b} \approx \sqrt{\left(\frac{R_w}{\sqrt{2}}\right)^4 + 1}. \quad (17)$$

Since WII injection requires high-current drivers with $I_b \gtrsim 8.5$ kA and the witness bunches are injected at a position yielding a high transformer ratio, Eq. (17) implies that the produced bunches feature currents of tens of kA resulting in an optimal beam loading and the consequent reduction of the energy spread. Since in addition the WII injected bunches are naturally of low emittance (Eq. (13)), the latter result implies that the WII produced bunches have a high normalized brightness $B_n \propto I_b/\epsilon_n^2$, which is comparable and might be superior to electron beams generated in state of the art facilities for FEL application (LCLS, XFEL, etc.), when operating at plasma densities of $n_0 = 10^{18}$ cm $^{-3}$ or higher.

VI. SELF-SIMILAR STAGING

As a consequence of this study, provided that the WII injected witness bunches are short, of low-emittance and of high-current, they fulfil the essential requirements to drive strong plasma waves in a higher density plasma. The field configuration in this new plasma stage, in which the witness beam acts as the driver, may again trigger WII injection from an appropriate dopant species. Given the driver in the first plasma stage was near to the resonance condition, $k_p \sigma_z \approx 1$, and the length of the produced witness is $k_p \sigma_z \sim 0.1$ (Eq. (13)), the density in the next plasma stage, in which the witness drives a resonant blowout wake, needs to be about 100 times greater than in the first stage. We can therefore formulate the following relation $n'_0/n_0 = (\sigma_z^b/\sigma_z^w)^2 \approx 100$, where n_0 and n'_0 are the densities of the first and second stage, respectively. Owing to the increased density, the witness bunches generated in the second plasma stage (where the previous witness bunch acts now as driver) will have a dramatically reduced size and normalized emittance. Using the scaling of the witness bunch properties (Eq. (13)), one can estimate a reduction of one order of magnitude in size and normalized emittance of the second witness beam with respect to the first, and an about two orders of magnitude increased normalized brightness ($B_n \propto I_b/\epsilon_n^2$). In addition, due to the high transformer ratio, the energy per electron of the second witness can be double or thrice the one in the first witness. This means, an increase of up to one order of magnitude in the energy per electron of the second witness with respect to the first driver. This is a novel concept of self-similar staging in PWFA, in which every next stage operates in a significantly increased plasma density.

We have explored the validity of this new concept of staging using PIC simulations in the same manner as we did in Secs. III and IV. In this case we used as driver an electron beam with exactly the same statistical properties as the witness beam in the beam-loaded FACET case (Figure 13 (c) and (d)). The field structure of this driver operating in a plasma with $n_0 = 4 \times 10^{19}$ cm $^{-3}$ density allows for WII injection from an appropriate ionization level at the required ionization threshold. In this particular example, the fifth ionization level of neon, with an ionization threshold of $E_{\text{ion}} = 557$ GV/m fulfills the condition expressed in Eq. (3) (cf. Figure 2). The witness bunches generated in this second plasma stage feature ultra-short durations (100 as (rms)), and ultra-low normalized emittances (60 nm), while exhibiting high-currents (15 kA) for a proper beam loading. Provided that the normalized emittance of the second witness is about 20 times smaller than the first witness, and that the peak current is essentially the same, the peak normalized brightness of the second witness bunch in respect to the first is about 400 times higher. Such values would largely exceed those from state of the art conventional linear electron accelerators. Furthermore, provided that the beam is injected in a phase position such that the

transformer ratio is around 3, its final energy after two stages could exceed 100 GeV per electron, if the self-similar staging process is initiated by the 23 GeV FACET electron beam.

The same concept of staging can be applied to electron bunches produced in laser-driven plasma wakefield accelerators (LWFA), as they could have enough current^{49,50} to drive strong plasma wakes and trigger WII injection in a second plasma stage of increased density (PWFA). A similar hybrid staging concept was proposed as a way of producing, from a LWFA stage, driver/witness electron beam pairs that can operate a PWFA stage at higher plasma densities than driver/witness pairs from conventional accelerators⁵¹. Here, we propose to use just one high-current LWFA produced electron beam that drives strong plasma wakes at (or near) the resonant density, and injects its own high-quality witness bunch by means of the WII injection mechanism. The requirements for WII injection are mainly demanding on the current profile of the beam, but not too strict in terms of emittance and energy spread. This makes electron beams generated in LWFA experiments suitable candidates to drive the WII injection mechanism in a significantly increased density plasma stage, for the creation of ultra-short, low-emittance and high-current electron beams with multi-GeV energy in a room the size of a laser lab.

VII. SUMMARY

The WII injection technique requires high-current ($I_b \gtrsim 8.5$ kA) and moderate length ($L_b \approx \lambda_p$) drive beams, to generate plasma waves in a strong blowout regime. In this regime the plasma wake is capable of trapping electrons from ionization. The drive beams need to be smaller transversely in the high-current region than the blowout radius ($k_p \sigma_r < k_p r_m \approx 2\sqrt{\Lambda_b}$) to excite the plasma wave most efficiently and to transport the beam, but wide enough to obtain a maximum radial electric field below the ionization threshold in the region of the driver ($k_p \sigma_r > 0.63 \sqrt{\Lambda_b}$). Moreover, the driver's beta function needs to be greater than the matched beta in the focusing ion channel, so that the driver beam is transversely compressed after the injection to ensure a stable propagation that mitigates the head erosion. This sets a condition for the beam transverse emittance $k_p \epsilon_n < \sqrt{\gamma}/2 (k_p \sigma_r)^2$. By a proper choice of the HIT dopant species, the wakefield induces injection and trapping from a restricted phase-space area at the back of the first plasma bucket. The electron bunches injected by means of the WII injection method have, by construction, a characteristic size and a normalized emittance of the order of a fraction of the plasma skindepth. This means sub-micron length and emittance for densities close to 10^{18} cm^{-3} . Because the phase of injection is located near to the end of the cavity, the WII injected witness beams are accelerated at (or close to) the optimal phase of the plasma wake, where the accelerating gradients are the highest and the trans-

verse fields are focusing. The requirements for WII injection comply with those for an efficient operating mode of the PWFA³⁸, providing the best driver-to-witness energy exchange (i.e. the highest transformer ratio). This injection strategy results in a controlled beam loading to flatten the accelerating field along the witness bunch length, which leads to a significant reduction of the energy spread.

The required witness currents for optimized beam loading are on the order of tens of kA. As a result, the WII injection can produce high-quality electron bunches with short pulse length, low normalized emittance, high-current, high-brightness and low-energy spread, with an energy per electron of around three times that of the drive beam. This can be achieved in a relatively simple experimental setup.

The witness bunches generated by the above process fulfil all requirements to again trigger WII injection as driver beams in substantially higher-density plasmas. This new concept of self-similar staging has the potential to produce electron beams with unprecedented energy and quality in PWFA.

ACKNOWLEDGMENTS

We thank the OSIRIS consortium (IST/UCLA) for access to the OSIRIS code. Special thanks for support go to J. Vieira and R. Fonseca. Furthermore, we acknowledge the grant of computing time by the Jülich Supercomputing Centre on JUQUEEN under Project No. HHH23 and the use of the High-Performance Cluster (IT-HPC) at DESY. This work was funded by the Humboldt Professorship of B. Foster, the Helmholtz Virtual Institute VH-VI-503 and ARD program.

REFERENCES

- ¹A. Martinez de la Ossa, J. Grebenyuk, T. Mehrling, L. Schaper, and J. Osterhoff, *Phys. Rev. Lett.* **111**, 245003 (2013).
- ²V. Veksler, Proceedings of CERN Symposium on High Energy Accelerators and Pion Physics **1**, 80 (1956).
- ³P. Chen, J. M. Dawson, R. W. Huff, and T. Katsouleas, *Phys. Rev. Lett.* **54**, 693 (1985).
- ⁴I. Blumenfeld, C. E. Clayton, F.-J. Decker, M. J. Hogan, C. Huang, R. Ischebeck, R. Iverson, C. Joshi, T. Katsouleas, N. Kirby, W. Lu, K. A. Marsh, W. B. Mori, P. Muggli, E. Oz, R. H. Siemann, D. Walz, and M. Zhou, *Nature* **445**, 741 (2007).
- ⁵T. Tajima and J. M. Dawson, *Phys. Rev. Lett.* **43**, 267 (1979).
- ⁶S. P. D. Mangles, C. D. Murphy, Z. Najmudin, A. G. R. Thomas, J. L. Collier, A. E. Dangor, E. J. Divall, P. S. Foster, J. G. Gallacher, C. J. Hooker, D. A. Jaroszynski, A. J. Langley, W. B. Mori, P. A. Norreys, F. S. Tsung, R. Viskup, B. R. Walton, and K. Krushelnick, *Nature* **431**, 535 (2004).
- ⁷C. G. R. Geddes, C. Toth, J. van Tilborg, E. Esarey, C. B. Schroeder, D. Bruhwiler, C. Nieter, J. Cary, and W. P. Lee-mans, *Nature* **431**, 538 (2004).
- ⁸J. Faure, Y. Glinec, A. Pukhov, S. Kiselev, S. Gordienko, E. Lefebvre, J. P. Rousseau, F. Burgy, and V. Malka, *Nature* **431**, 541 (2004).

- ⁹T.-Y. Chien, C.-L. Chang, C.-H. Lee, J.-Y. Lin, J. Wang, and S.-Y. Chen, *Phys. Rev. Lett.* **94**, 115003 (2005).
- ¹⁰J. Faure, C. Rechatin, A. Norlin, A. Lifschitz, Y. Glinec, and V. Malka, *Nature* **444**, 737 (2006).
- ¹¹C. Rechatin, J. Faure, A. Ben-Ismaïl, J. Lim, R. Fitour, A. Specka, H. Videau, A. Tafzi, F. Burgy, and V. Malka, *Phys. Rev. Lett.* **102**, 164801 (2009).
- ¹²A. Pak, K. A. Marsh, S. F. Martins, W. Lu, W. B. Mori, and C. Joshi, *Phys. Rev. Lett.* **104**, 025003 (2010).
- ¹³C. McGuffey, A. G. R. Thomas, W. Schumaker, T. Matsuoka, V. Chvykov, F. J. Dollar, G. Kalintchenko, V. Yanovsky, A. Maksimchuk, K. Krushelnick, V. Y. Bychenkov, I. V. Glazyrin, and A. V. Karpeev, *Phys. Rev. Lett.* **104**, 025004 (2010).
- ¹⁴C. E. Clayton, J. E. Ralph, F. Albert, R. A. Fonseca, S. H. Glenzer, C. Joshi, W. Lu, K. A. Marsh, S. F. Martins, W. B. Mori, A. Pak, F. S. Tsung, B. B. Pollock, J. S. Ross, L. O. Silva, and D. H. Froula, *Phys. Rev. Lett.* **105**, 105003 (2010).
- ¹⁵A. J. Gonsalves, K. Nakamura, C. Lin, D. Panasenkov, S. Shiraishi, T. Sokollik, C. Benedetti, C. B. Schroeder, C. G. R. Geddes, J. van Tilborg, J. Osterhoff, E. Esarey, C. Toth, and W. P. Leemans, *Nature Physics* **7**, 862 (2011).
- ¹⁶D. Umstadter, J. K. Kim, and E. Dodd, *Phys. Rev. Lett.* **76**, 2073 (1996).
- ¹⁷E. Esarey, R. F. Hubbard, W. P. Leemans, A. Ting, and P. Sprangle, *Phys. Rev. Lett.* **79**, 2682 (1997).
- ¹⁸S. Bulanov, N. Naumova, F. Pegoraro, and J. Sakai, *Phys. Rev. E* **58**, R5257 (1998).
- ¹⁹M. Chen, E. Esarey, C. B. Schroeder, C. G. R. Geddes, and W. P. Leemans, *Physics of Plasmas* **19**, 033101 (2012).
- ²⁰M. J. Hogan, C. D. Barnes, C. E. Clayton, F. J. Decker, S. Deng, P. Emma, C. Huang, R. H. Iverson, D. K. Johnson, C. Joshi, T. Katsouleas, P. Krejcik, W. Lu, K. A. Marsh, W. B. Mori, P. Muggli, C. L. O'Connell, E. Oz, R. H. Siemann, and D. Walz, *Phys. Rev. Lett.* **95**, 054802 (2005).
- ²¹M. Litos, E. Adli, W. An, C. I. Clarke, C. E. Clayton, S. Corde, J. P. Delahaye, R. J. England, A. S. Fisher, J. Frederico, S. Gessner, S. Z. Green, M. J. Hogan, C. Joshi, W. Lu, K. A. Marsh, W. B. Mori, P. Muggli, N. Vafaei-Najafabadi, D. Walz, G. White, Z. Wu, V. Yakimenko, and G. Yocky, *Nature* **515**, 92 (2014).
- ²²H. Suk, N. Barov, J. B. Rosenzweig, and E. Esarey, *Phys. Rev. Lett.* **86**, 1011 (2001).
- ²³J. Vieira, S. F. Martins, V. B. Pathak, R. A. Fonseca, W. B. Mori, and L. O. Silva, *Phys. Rev. Lett.* **106**, 225001 (2011).
- ²⁴E. Oz, S. Deng, T. Katsouleas, P. Muggli, C. D. Barnes, I. Blumenfeld, F. J. Decker, P. Emma, M. J. Hogan, R. Ischebeck, R. H. Iverson, N. Kirby, P. Krejcik, C. O'Connell, R. H. Siemann, D. Walz, D. Auerbach, C. E. Clayton, C. Huang, D. K. Johnson, C. Joshi, W. Lu, K. A. Marsh, W. B. Mori, and M. Zhou, *Phys. Rev. Lett.* **98**, 084801 (2007).
- ²⁵N. Kirby, I. Blumenfeld, C. E. Clayton, F. J. Decker, M. J. Hogan, C. Huang, R. Ischebeck, R. H. Iverson, C. Joshi, T. Katsouleas, W. Lu, K. A. Marsh, S. F. Martins, W. B. Mori, P. Muggli, E. Oz, R. H. Siemann, D. R. Walz, and M. Zhou, *Phys. Rev. ST Accel. Beams* **12**, 051302 (2009).
- ²⁶M. J. Hogan, T. O. Raubenheimer, A. Seryi, P. Muggli, T. Katsouleas, C. Huang, W. Lu, W. An, K. A. Marsh, W. B. Mori, C. E. Clayton, and C. Joshi, *New Journal of Physics* **12**, 055030 (2010).
- ²⁷N. Vafaei-Najafabadi, K. A. Marsh, C. E. Clayton, W. An, W. B. Mori, C. Joshi, W. Lu, E. Adli, S. Corde, M. Litos, S. Li, S. Gessner, J. Frederico, A. S. Fisher, Z. Wu, D. Walz, R. J. England, J. P. Delahaye, C. I. Clarke, M. J. Hogan, and P. Muggli, *Phys. Rev. Lett.* **112**, 025001 (2014).
- ²⁸B. Hidding, G. Pretzler, J. B. Rosenzweig, T. Königstein, D. Schiller, and D. L. Bruhwiler, *Phys. Rev. Lett.* **108**, 035001 (2012).
- ²⁹F. Li, J. F. Hua, X. L. Xu, C. J. Zhang, L. X. Yan, Y. C. Du, W. H. Huang, H. B. Chen, C. X. Tang, W. Lu, C. Joshi, W. B. Mori, and Y. Q. Gu, *Phys. Rev. Lett.* **111**, 015003 (2013).
- ³⁰J. Rosenzweig, B. Breizman, T. C. Katsouleas, and J. Su, *Phys. Rev. A* **44**, 6189 (1991).
- ³¹K. Lotov, *Phys. Rev. E* **69**, 046405 (2004).
- ³²W. Lu, C. Huang, M. Zhou, W. B. Mori, and T. Katsouleas, *Phys. Rev. Lett.* **96**, 165002 (2006).
- ³³R. A. Fonseca, L. O. Silva, F. S. Tsung, V. K. Decyk, W. Lu, C. Ren, W. Mori, S. Deng, S. Lee, T. Katsouleas, and J. Adam, *Notes Comp. Sci.* **2331**, 342 (2002).
- ³⁴R. A. Fonseca, S. F. Martins, L. O. Silva, J. W. Tonge, F. S. Tsung, and W. B. Mori, *Plasma Physics and Controlled Fusion* **50**, 124034 (2008).
- ³⁵R. A. Fonseca, J. Vieira, F. Fiuza, A. Davidson, F. S. Tsung, W. B. Mori, and L. O. Silva, *Plasma Physics and Controlled Fusion* **55**, 124011 (2013).
- ³⁶J. M. Dawson, *Phys. Rev.* **113**, 383 (1959).
- ³⁷P. Chen, J. Su, J. Dawson, K. Bane, and P. B. Wilson, *Phys. Rev. Lett.* **56**, 1252 (1986).
- ³⁸K. V. Lotov, *Physics of Plasmas* **12**, 053105 (2005).
- ³⁹A. Perelomov, V. Popov, and M. Terentev, *JETP* **23**, 924 (1966).
- ⁴⁰M. V. Ammosov, N. B. Delone, and V. Krainov, *Sov. Phys. JETP* **64**, 1191 (1986).
- ⁴¹C. E. Clayton, B. E. Blue, E. S. Dodd, C. Joshi, K. A. Marsh, W. B. Mori, S. Wang, P. Catravas, S. Chattopadhyay, E. Esarey, W. P. Leemans, R. Assmann, F. J. Decker, M. J. Hogan, R. Iverson, P. Raimondi, R. H. Siemann, D. Walz, T. Katsouleas, S. Lee, and P. Muggli, *Phys. Rev. Lett.* **88**, 154801 (2002).
- ⁴²E. Esarey, B. A. Shadwick, P. Catravas, and W. P. Leemans, *Phys. Rev. E* **65**, 056505 (2002).
- ⁴³P. Sprangle, E. Esarey, and A. Ting, *Phys. Rev. Lett.* **64**, 2011 (1990).
- ⁴⁴W. An, M. Zhou, N. Vafaei-Najafabadi, K. A. Marsh, C. E. Clayton, C. Joshi, W. B. Mori, W. Lu, E. Adli, S. Corde, M. Litos, S. Li, S. Gessner, J. Frederico, M. J. Hogan, D. Walz, J. England, J. P. Delahaye, and P. Muggli, *Phys. Rev. ST Accel. Beams* **16**, 101301 (2013).
- ⁴⁵W. Lu, C. Huang, M. M. Zhou, W. B. Mori, and T. Katsouleas, *Physics of Plasmas* **12**, 063101 (2005).
- ⁴⁶P.-F. Hao, Y.-T. Ding, Z.-H. Yao, F. He, and K.-Q. Zhu, *J. Micromech. Microeng.* **15**, 2069 (2005).
- ⁴⁷L. Schaper, L. Goldberg, T. Kleinwächter, J.-P. Schwinkendorf, and J. Osterhoff, *Nucl. Instrum. Meth.* **A740**, 208 (2014).
- ⁴⁸M. Tzoufras, W. Lu, F. S. Tsung, C. Huang, W. B. Mori, T. Katsouleas, J. Vieira, R. A. Fonseca, and L. O. Silva, *Phys. Rev. Lett.* **101**, 145002 (2008).
- ⁴⁹S. M. Wiggins, R. C. Issac, G. H. Welsh, E. Brunetti, R. P. Shanks, M. P. Anania, S. Cipiccia, G. G. Manahan, C. Aniculaesei, B. Ersfeld, M. R. Islam, R. T. L. Burgess, G. Vieux, W. A. Gillespie, A. M. MacLeod, S. B. van der Geer, M. J. de Loos, and D. A. Jaroszynski, *Plasma Physics and Controlled Fusion* **52**, 124032 (2010).
- ⁵⁰O. Lundh, J. Lim, C. Rechatin, L. Ammoura, A. Ben-Ismaïl, X. Davoine, G. Gallot, J.-P. Goddet, E. Lefebvre, V. Malka, and J. Faure, *Nat Phys* **7**, 219 (2011).
- ⁵¹B. Hidding, T. Königstein, J. Osterholz, S. Karsch, O. Willi, and G. Pretzler, *Phys. Rev. Lett.* **104**, 195002 (2010).